JGR Space Physics

RESEARCH ARTICLE
10.1029/2020JA029086

Special Section:
Geospace multi-point observations in Van Allen Probes and Arase era

First Simultaneous Observation of a Night Time Medium-Scale Traveling Ionospheric Disturbance From the Ground and a Magnetospheric Satellite

K. Kawai[1], K. Shiokawa[1], Y. Otsuka[1], S. Oyama[1,2], Y. Kasaba[3], Y. Kasahara[4], F. Tsuchiya[3], A. Kumamoto[3], S. Nakamura[1], A. Matsuoka[5], S. Imajo[5], Y. Kazama[6], S.-Y. Wang[6], S. W. Y. Tam[7], T. F. Chang[7], B. J. Wang[6], K. Asamura[8], S. Kasahara[9], S. Yokota[10], K. Keika[9], T. Hori[1], Y. Miyoshi[1], C. Jun[1], M. Shoji[1], and I. Shinohara[8]

[1]Institute for Space-Earth Environmental Research, Nagoya University, Nagoya, Japan, [2]National Institute of Polar Research, Tokyo, Japan, [3]Tohoku University, Sendai, Japan, [4]Kanazawa University, Kanazawa, Japan, [5]Kyoto University, Kyoto, Japan, [6]Academia Sinica Institute of Astronomy and Astrophysics, Taipei, Taiwan, [7]National Cheng Kung University, Tainan, Taiwan, [8]Institute of Space and Astronautical Science, Japan Aerospace Exploration Agency, Sagamihara, Japan, [9]University of Tokyo, Tokyo, Japan, [10]Osaka University, Toyonaka, Japan

Key Points:

- First simultaneous observation of an medium-scale traveling ionospheric disturbance (MSTID) using a ground-based airglow imager and the Arase satellite in the magnetosphere
- The polarization electric field associated with the MSTID in the ionosphere was projected to the magnetosphere and observed by Arase
- The electric field and electron density observed by the Arase satellite showed a periodic variation associated with the MSTID structure

Correspondence to:
K. Kawai,
kawai.kouki@isee.nagoya-u.ac.jp

Citation:
Kawai, K., Shiokawa, K., Otsuka, Y., Oyama, S., Kasaba, Y., Kasahara, Y., et al. (2021). First simultaneous observation of a night time medium-scale traveling ionospheric disturbance from the ground and a magnetospheric satellite. *Journal of Geophysical Research: Space Physics*, *126*, e2020JA029086. https://doi.org/10.1029/2020JA029086

Received 28 DEC 2020
Accepted 7 JUL 2021

Abstract Medium-scale traveling ionospheric disturbances (MSTIDs) are a phenomenon widely and frequently observed over the ionosphere from high to low latitudes. Night time MSTIDs are caused generally by the polarization electric field in the ionosphere. However, propagation of this polarization electric field to the magnetosphere has not yet been identified. Here, we report the first observation of the polarization electric field and associated density variations of a night time MSTID in the magnetosphere. The MSTID event was observed by an all-sky airglow imager at Gakona (geographical latitude: 62.39°N, geographical longitude: 214.78°E, magnetic latitude: 63.20°N), Alaska. The Arase satellite passed over the MSTID in the inner magnetosphere at 0530–0800 UT (2030–2300 LT) on November 3, 2018. This MSTID, observed in 630 nm airglow images, was propagating westward with a horizontal wavelength of ~165 km, a north–south phase front, and a phase velocity of ~80 m/s. The Arase satellite footprint on the ionosphere crossed the MSTID in the direction nearly perpendicular to the MSTID phase fronts. The electric field and electron density observed by the Arase satellite showed periodic variation associated with the MSTID structure with amplitudes of ~2 mV/m and ~150 cm^{-3}, respectively. The electric field variations projected to the ionosphere are mainly in the east-west direction and are consistent with the direction of the polarization electric field expected from MSTID growth by $E \times B$ drift. This observation indicates that the polarization electric field associated with the MSTID in the ionosphere is projected onto the magnetosphere, causing plasma density fluctuations in the magnetosphere.

Plain Language Summary Medium-scale traveling ionospheric disturbances (MSTIDs) are propagation of electron density fluctuation in the ionospheric F-layer. MSTIDs are a common phenomenon from high to low latitudes. From simultaneous observations of airglow imagers in both hemispheres, MSTIDs are known to have a mirror structure at magnetic conjugate hemispheres. If an MSTID is generated by ionospheric instabilities, the polarization electric field associated with the MSTID should propagate along the magnetic field lines. In this paper, we report the first simultaneous observation of an MSTID using a ground-based airglow imager and the Arase satellite in the magnetosphere. The electric field variations and plasma density fluctuations observed by Arase showed periodic variations associated with the MSTID structure. This result indicates that the spatial inhomogeneity of the ionospheric Pedersen conductivity associated with the MSTID yields the polarization electric field in the ionosphere, and that this polarization electric field was projected onto the magnetosphere.

1. Introduction

Traveling ionospheric disturbances (TIDs) are wave-like variations of plasma density propagating in the F region of the ionosphere. TIDs are classified by their velocity, wavelength, and period. Medium-scale traveling ionospheric disturbances (MSTIDs) have phase velocities, wavelengths, and periods of ~100–250 m/s, several hundred kilometers, and ~15–60 min (Hunsuker, 1982). Since an MSTID is a fluctuation of plasma

density in the ionosphere, it can be observed as variations in airglow emission intensity at a wavelength of 630.0 nm, which is excited by interaction of atomic oxygen ions and oxygen molecules in the F-region ionosphere with an emission altitude of 200–300 km.

There are two theories regarding the generation mechanisms of MSTIDs. One is that disturbance in the lower atmosphere propagates upward as atmospheric gravity waves and causes plasma fluctuation in the ionosphere (e.g., Hines, 1960; Hooke, 1968). The other is that they are generated by ionospheric E-region–F-region (E–F) coupling instability with Perkins instability caused by the unstable state of plasma in the E- and F-region ionosphere (e.g., Cosgrove & Tsunoda, 2001; Perkins, 1973). At mid-latitudes in the northern (southern) hemisphere, night time MSTIDs have a northwest–southeast (northeast–southwest) phase front, and propagate southwestward (northwestward) (e.g., Figueiredo et al., 2018; Garcia et al., 2000; Martinis et al., 2010; Otsuka et al., 2013; Shiokawa, Ihara, et al., 2003). This feature of the phase front can be explained by the fact that MSTIDs are generated by the E–F coupling and Perkins instabilities, where the sporadic-E (Es) layer combines with the F layer and causes dramatic growth of MSTIDs. The characteristic of southwestward (northwestward) propagation in the northern (southern) hemisphere (Fukao et al., 1991; Shiokawa, Otsuka, et al., 2003) can be explained by the southward (northward) wind is induced in the Es layer (Yokoyama et al., 2009).

The polarization electric field associated with this type of MSTID is expected to propagate along magnetic field lines from one hemisphere to the other due to the high electrical conductivity in the direction along the magnetic field lines. The interhemispheric propagation has been confirmed by simultaneous observations of the ground airglow imagers in both hemispheres where the MSTIDs in the middle latitude have a mirror image structure at the magnetic conjugate point (e.g., Martinis et al., 2017; Otsuka et al., 2004; Shiokawa et al., 2005). Therefore, if an MSTID is generated by ionospheric plasma instabilities and grows with a polarization electric field structure, this polarization electric field possibly propagates along the magnetic field line, and even satellites in the inner magnetosphere should be able to observe electric field variations. However, no simultaneous observations of MSTIDs by satellites in the inner magnetosphere have yet been reported. Such simultaneous measurements in the inner magnetosphere will provide information on how the signatures of MSTIDs propagate along magnetic field line and how the MSTIDs cause disturbances in the magnetospheric plasma.

In this paper, we report the first observation of polarization electric field and electron density fluctuations in the magnetosphere associated with an MSTID event observed through 630.0 nm night time airglow images acquired on the ground and the Arase satellite (Miyoshi, Shinohara, Takashima, et al., 2018) passing through the magnetosphere. This observation shows that ionospheric plasma disturbances can generate plasma structures in the magnetosphere through the polarization electric field, and vice versa.

2. Airglow Observations

The all-sky airglow imager at Gakona (geographical latitude: 62.39°N, geographical longitude: 214.78°E, magnetic latitude: 63.20°N) is one of the Optical Mesosphere Thermosphere Imagers (OMTIs) (Shiokawa et al., 1999). It has a fisheye lens with a 180° field-of-view, five band-pass filters of different wavelengths, and a 1024 × 1024-pixel back-illuminated cooled-CCD camera. To increase the output count, raw counts are summed for 2 × 2 bins to give images of 512 × 512 pixels. The band-pass filters for wavelengths of 557.7, 630.0, and 572.5 nm have transmission band-widths of 1.781, 1.685, and 1.492 nm, respectively. Every 90 s, 557.7 and 630.0 nm airglow images were taken with exposure times of 15 and 30 s, respectively. This study used images obtained through these three band-pass filters. Shiokawa et al. (1999, 2017) described details of the all-sky airglow imager system.

Figure 1 shows an MSTID observed in the 630.0 nm airglow images acquired at Gakona on November 3, 2018. These images are mapped from all-sky (fish-eye) images into geographical coordinates with assuming an altitude of 250 km. The lens distortion of all-sky images is corrected when they are converted the images into geographical coordinates. The absolute intensity in Rayleigh units shown in Figure 1 was obtained by subtracting background sky emissions measured using the 572.5 nm filter, considering the difference in transmission widths of the 630.0 and 572.5 nm filters. Figure 1 shows nine images taken every 20 min from 0520:22 UT to 0800:22 UT. The red dashed lines and yellow dots represent the trajectory and instantaneous

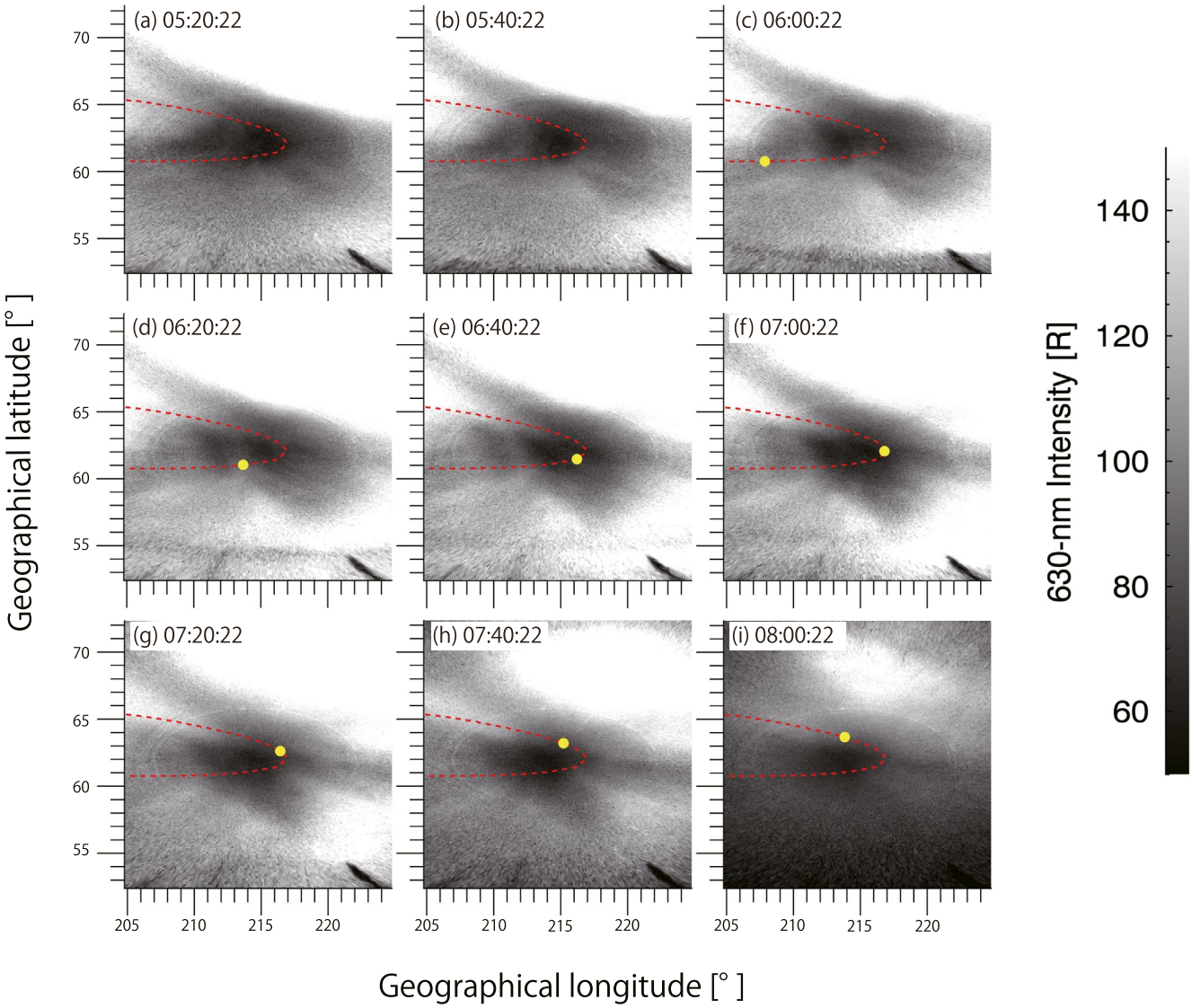

Figure 1. Airglow images at a 630.0 nm wavelength acquired from 0520:22 UT-0800:22 UT on November 3, 2018 at Gakona in geographical coordinates, assuming a 630.0 nm airglow emission altitude of 250 km. Red dashed lines and yellow dots indicate the satellite's orbit and the Arase satellite position, respectively, projected onto the ionosphere.

positions of the Arase satellite footprint, respectively, mapped to an altitude of 250 km in the ionosphere using the Tsyganenko–Sitnov 2005 (TS05) magnetic field model (Tsyganenko & Sitnov, 2005). If the assumed altitude is shifted by 50 km, the Arase satellite footprint shifts by ~13 km in the meridional direction because the inclination of the magnetic field at Gakona is 75.8°. The double elliptic circles seen near the image centers are artificial effects of the integrating sphere used for imager calibration.

In Figure 1, the aurora at the equatorward part of the auroral oval was continuously seen in the northeast part of these images. The MSTID is difficult to be recognized but is seen equatorward the auroral oval mainly in the western half of these images. The next figure shows the MSTID structure more clearly.

Figure 2 shows 630.0 nm images obtained by subtracting 1 h running averages of emission intensity from raw images to clearly show the MSTID structure. The image acquisition times are the same as in Figure 1. The color scale represents airglow deviation $\Delta I(t)$, defined as $\Delta I(t) = [\{I(t) - I_a(t)\}/I_a(t)] \times 100$ for each image pixel, where $I(t)$ is the airglow intensity at time t, and $I_a(t)$ is the average airglow intensity over $t \pm 30$ min. In Figure 2, the ionospheric footprint trajectory and the Arase satellite positions are overlaid by

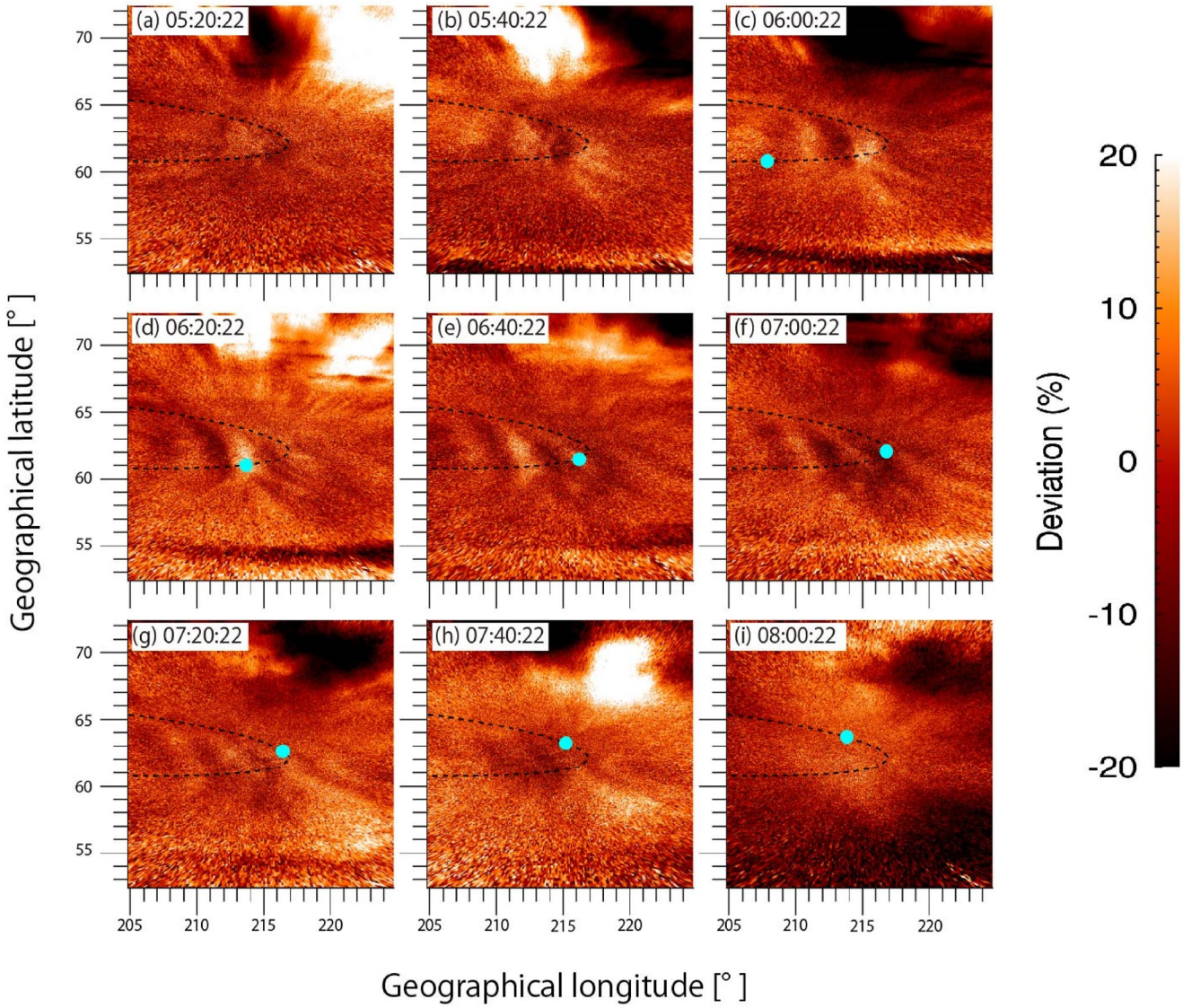

Figure 2. 630.0 nm airglow deviation images obtained by subtracting 1 h running averages. These images are shown in geographical coordinates. Black dashed lines and cyan dots indicate the orbit and position of the Arase satellite, respectively, projected onto the ionosphere.

black dashed curves and cyan dots, respectively. These images are shown in latitude-longitude axes. Thus we should note that the true east-west distance at the high latitude boundary (72.39°N) of these images is about half of that of the low latitude boundary (52.39°N). Therefore, if the phase front propagates at the same direction and velocity in the real world, the high latitude portion moves zonally faster than that of low latitude in Figure 2. This could lead to an apparent rotation of N-S front of the MSTID at the center to NW-SE as it travels westward.

Figures 2b–2g, clearly show that the north–south wave structure of the MSTID at 59–65°N and 205–220°E propagates westward. The MSTID phase front gradually rotates from the north–south to the northwest–southeast orientation. The Arase satellite footprints crossed the phase fronts nearly perpendicularly at 0600–0700 UT and afterward moved westward along the phase fronts of the MSTID. After ~0740 UT, the MSTID was not visible owing to clouds over Gakona.

Figure 3 shows east-west cross sections (keograms) of the 630.0 nm and 557.7 nm airglow intensities and their deviations as defined in the previous figure to clarify wave characteristics of the MSTID. Figures 3a–3d show east-west keograms taken at 62.40°N (Gakona latitude) for (a) 630.0 nm airglow intensity, (b) 630.0 nm

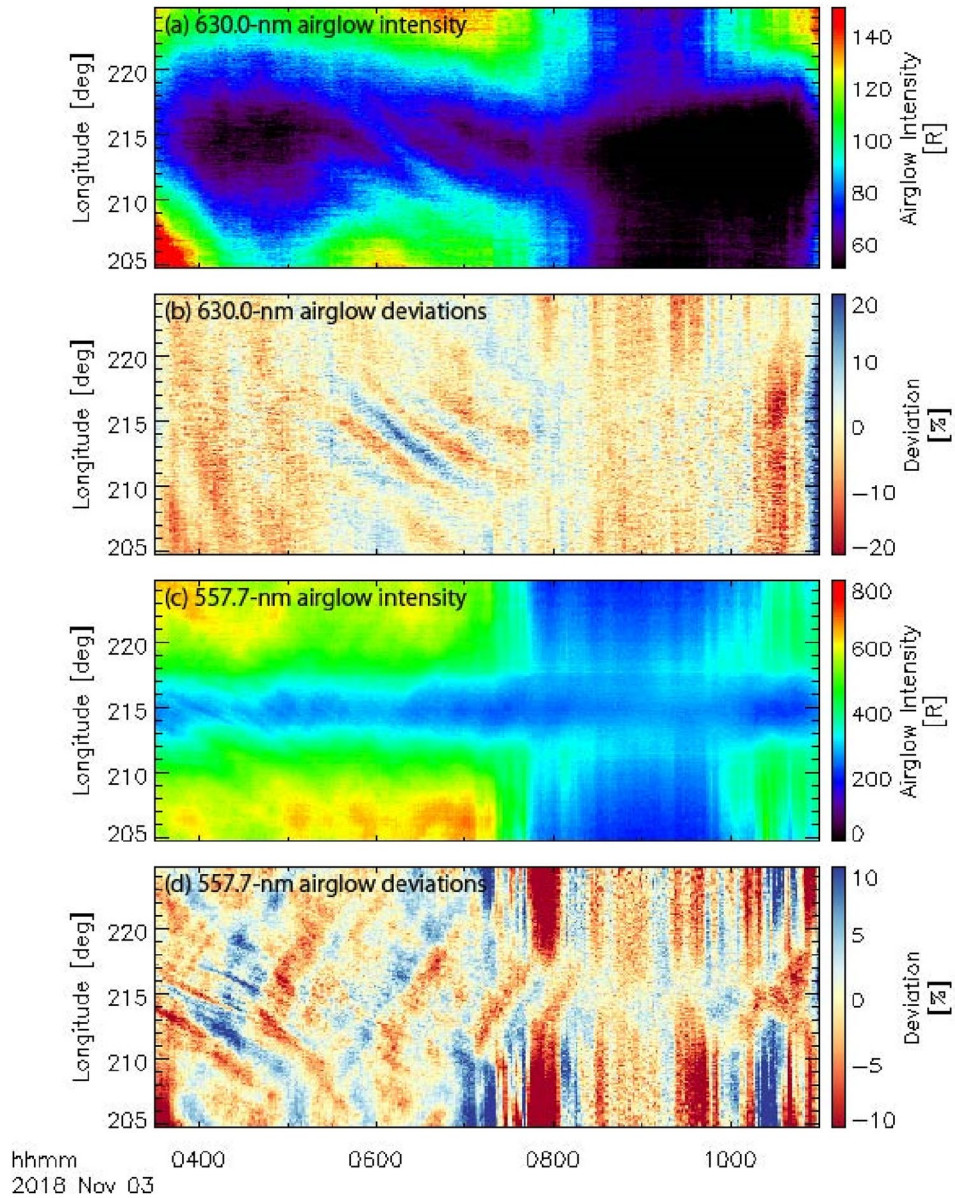

Figure 3. East-west cross sections (keograms) of airglow images at the Gakona latitude (62.40°N) in geographical coordinates, observed on November 3, 2018 at Gakona. These keograms represent (a) 630.0 nm airglow intensity, (b) 630.0 nm airglow deviations from 1 h running averages, (c) 557.7 nm airglow intensity, and (d) 557.7 nm airglow deviations from 1 h running averages. The vertical axis shows geographical east longitude, and the horizontal axis shows UT.

airglow deviations, (c) 557.7 nm airglow intensity, and (d) 557.7 nm airglow deviations. The 630.0 nm and 557.7 nm images were mapped to geographic coordinates assuming airglow altitudes of 250 and 100 km, respectively. In Figure 3, the vertical axis represents geographical longitude, and the horizontal axis represents time in UT.

Figures 3a and 3b clearly show westward MSTID propagation at ~208–218°E from 0530–0745 UT. From Figure 3b, we estimate an MSTID wavelength of ~165 km and a period of ~1 h, and calculated the phase velocity of ~80 m/s, all these are estimated for zonal direction considering that the MSTID phase front is basically north-south. These values roughly match the characteristic MSTID parameters shown by Hunsuker (1982).

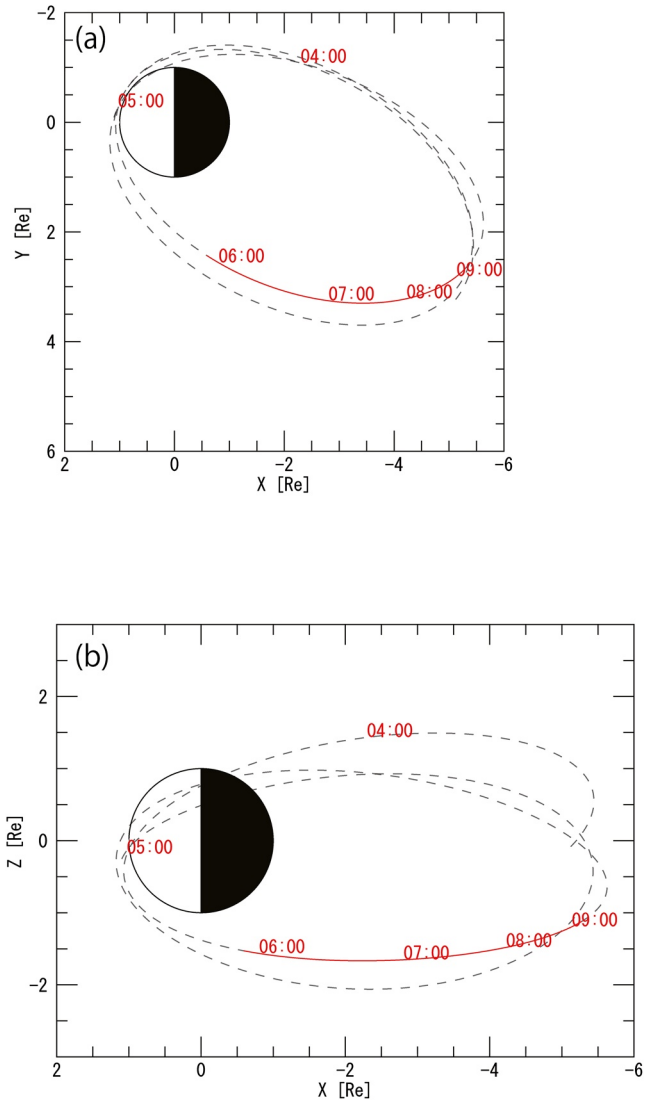

Figure 4. Arase satellite orbit (level 2/version 03) from 0000 to 2400 UT on November 3, 2018 for the (a) x–y plane and (b) x–z plane in solar magnetic (SM) coordinates. The red solid line shows times at which the Arase satellite footprint was in the field-of-view of the airglow imager at Gakona.

The structures in the 557.7 nm east-west keograms in Figures 3c and 3d move both eastward and westward at ~210–220°E from ~0330 to 0800 UT. We consider these structures as atmospheric gravity waves propagating at the 557.7 nm airglow altitude of 90–100 km. The 630.0 nm and 557.7 nm airglow images are completely different in terms of the wave surface direction. This fact provides a further support for our interpretation that the structure in the 630.0 nm images is an MSTID in the ionosphere, not an aurora caused by electron precipitation or a cloud passing over the camera. It also provides our interpretation that the gravity waves seen in 577.7 nm images were not the seed of the MSTIDs seen in 630.0 nm images.

3. Satellite Observations

Figure 4 shows the Arase satellite orbit (Miyoshi, Shinohara, & Jun, 2018) on November 3, 2018 on (a) the x–y plane and (b) x–z plane in the solar magnetic (SM) coordinates system. The dashed curves show the Arase satellite orbit from 0000 to 2400 UT on November 3, 2018, and the red solid curves show that from 0554:36 to 0912:36 UT, when the Arase satellite was in the field of view of the airglow imager at Gakona (52.39–72.39°N, 204.78–224.78°E). The Arase satellite passed over at a radial distance of ~3–5 R_E in the late evening sector at 0600–0700 UT when the satellite footprint crossed the MSTID in the airglow images. Arase satellite data shown in this paper were analyzed using the Space Physics Environment Data Analysis Software (SPEDAS) tool (Angelopoulos et al., 2019).

Figure 5 shows (a) electric field spectra obtained by the High Frequency Analyzer (HFA) of the Plasma Wave Experiment (PWE) (Kasahara, Kumamoto, et al., 2018), (b) electric field spectra obtained by the Onboard Frequency Analyzer (OFA) of the PWE (Kasahara, Kojima, et al., 2018) (c) electron density, (d) electron number flux of MEP-e (Kasahara, Yokota, et al., 2018), (e) electron number flux of LEP-e (Wang et al., 2018), (f) proton differential number flux of MEP-i (Yokota et al., 2018), (g) proton differential number flux of LEP-i (Asamura et al., 2018), (h) magnetic field in SM coordinates measured by the MGF instrument (Matsuoka et al., 2018a, 2018b), and (i) electric field in SM coordinates measured by the u-sensor of EFD (Kasahara, Kasaba, et al., 2018), all onboard Arase. The electron density of Figure 5c was calculated from the upper-limit frequency of upper hybrid resonance (UHR) waves appearing in the spectra of Figure 5a. The magnetic field magnitude of MGF level-2 data was used to calculate the local electron gyro-frequency. The labels below the horizontal axis indicate the McIlwain L value derived from the IGRF-13 model (Bärenzung et al., 2020), magnetic local time, magnetic latitude (MLAT), radial distance from Earth (R_E), and time (UT). The black vertical dashed lines indicate the time period during which the satellite was in the field-of-view of the airglow imager (0554:36–0912:36 UT).

Figure 5c shows no rapid density decrease (plasmapause), usually occurring around $L = 4$, making it unclear whether the Arase satellite stayed inside or outside the plasmasphere when the satellite crossed the MSTID. However, the Arase satellite might stay in the plasmasphere, because plasmaspheric hiss was observed at ~0400–0700 UT below 1 kHz in Figure 5b, and lightning whistler waves were observed at, for example, 0605, 0615, and 0630 UT at ~10 kHz (identified in an unshown expanded version of Figure 5a). During 0400–0600 UT, the magnetic field and electric field in Figures 5h and 5i were very large, because the satellite was near perigee. The electron spectra in Figures 5d and 5e show that the satellite might be traversing the ring current region near the inner boundary of a plasma sheet, as three energy-time dispersion

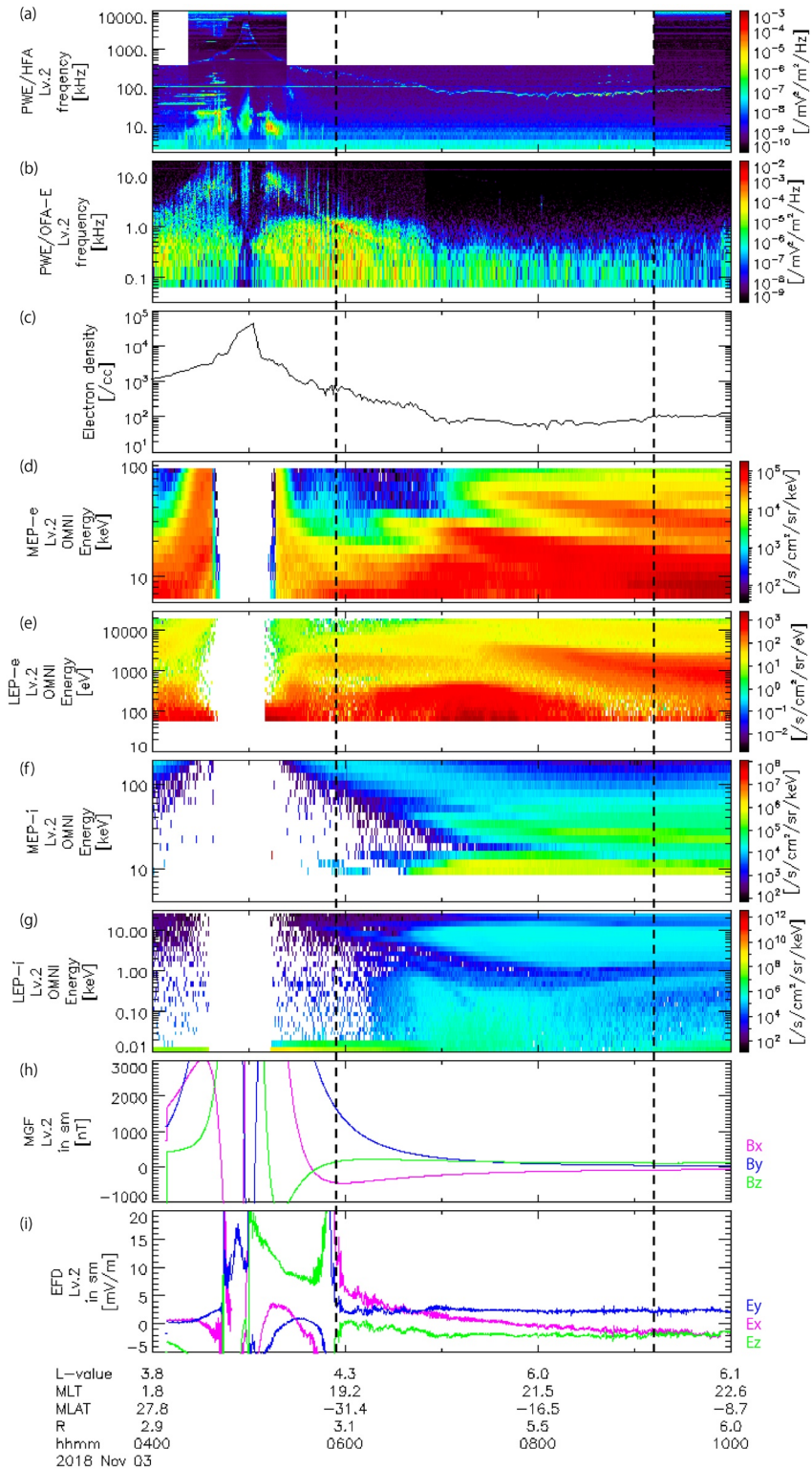

Figure 5. Data obtained by the Arase satellite on November 3, 2018. (a) Wave spectra (level 2/version 1.02) obtained from the Plasma Wave Experiment (PWE)/High Frequency Analyzer (HFA); (b) electric field spectra (level 2/version 2.01) obtained from the PWE/Onboard Frequency Analyzer (OFA); (c) electron density; (d) electron number flux obtained by MEP-e (level 2/version 1.02); (e) electron number flux obtained by LEP-e (level 2/version 2.02); (f) proton differential number flux obtained by MEP-i (level 2/version 2.00); (g) proton differential number flux obtained by LEP-i (level 2/version 3.00); (h) magnetic field (level 2/version 3.04) in solar magnetic (SM) coordinates; and (i) electric field measured by the u-sensor of EFD in SM coordinates (level 2/version 4.01). Black vertical dashed lines indicate the time interval during which the satellite was in the field-of-view of airglow imager.

structures (e.g., Ejiri et al., 1980; Smith & Hoffman, 1974) are seen at 0600–0900 UT. Similar structures are seen in the ion spectra in Figures 5f and 5g at 0600–0800 UT.

4. Comparison of Ground and Satellite Observations

In this section, we try to identify MSTID-related variations in electron densities, magnetic fields, and electric fields observed by the Arase satellite. Figure 6 shows (a) wave spectra, (b) electron density (Ne), (c) electric fields in SM coordinates, (d) electron density variations, (e) electric field variations (δE) in SM coordinates, and (f) 630.0-nm airglow deviations at the Arase satellite footprint. Variations in Figures 6d and 6e were calculated by subtracting 20 min running averages. Since the time interval that the Arase satellite pass through the peak-to-peak of the airglow intensity of the MSTID is 10–20 min, we apply the 20-min running average so that the waves in Figures 6d and 6e with periods of less than 20 min only can pass. The airglow deviations in Figure 6f were calculated by subtracting 1-h running averages in the airglow images. The horizontal axis is 0600–0700 UT, when the Arase satellite crossed the MSTID phase front. The angle between the satellite's spin plane and the local magnetic field varied from ∼10° at 0600 UT to ∼40° at 0700 UT. The vertical red and blue dashed lines show the time period during which the Arase satellite footprint passed through the bright and dark parts of the MSTID, respectively.

In Figure 6b, the electron density gradually decreases with time, because the satellite is moving from the evening to the night side away from Earth. The accuracy of manual determination of the UHR frequency is within 3 kHz and the resultant accuracy of Ne is within 12/cc. The electron densities in Figures 6b and 6d show variations with time scales of several minutes. These variations can be also recognized in the original UHR frequencies in Figure 6a. These density variations are not by the error of manual reading but real variations of the background density. The electron density variations in Figure 6d and the airglow deviations in Figure 6f clearly show an anticorrelation at ∼0610–0630 UT. After 0630 UT, the phase difference between them slightly deviates from the anticorrelation. We estimated their correlation coefficient as −0.508. The x- and y-component of the electric field variations in Figure 6e show a positive correlation with the airglow deviations, while the z-component shows a negative correlation. We calculate absolute values of electric field variations, and compare with airglow deviations, however, we do not see any clear correlations between them.

To confirm the reliability of electric field measurement, we also show the electric field vector in Despun Sun-sensor Inertia (DSI) coordinates, which is a satellite-based coordinate system. DSI-Z axis lies in the spin axis direction which is basically toward the sun. DSI-X points the sun sector direction in the spin plane perpendicular to the Z axis, which is detected by an onboard sun sensor for every spin. Then DSI-Y is defined as the cross product of the X- and Z-axes. Figure 7 shows (a) the electric field, (b) the residual magnetic field obtained by subtracting the IGRF model magnetic field from the observed magnetic field, (c) electric field variations (δE), (d) magnetic field variations (δB), and (e) the Poynting vector calculated from δE and δB. Figures 7a–7d are illustrated in DSI coordinates, and Figure 7e is illustrated in the field-aligned (FA) coordinate. FA-z is parallel to the direction of the background magnetic field (northward is positive), FA-y is in the plane perpendicular to FA-z and the vector of SM-x, and FA-x is the cross component of FA-y and FA-z. Figure 7b shows the residual magnetic field calculated by subtracting the IGRF model magnetic field. To eliminate the short-period oscillation (period: ∼1 min) seen in the electric field data in Figure 7a, we calculated 5 min running averages. Then 20 min running averages were further removed from the 5 min averages to show only electric field variations associated with the MSTID structure in Figure 7c. We performed the same filtering for the magnetic field data in Figure 7d. Again, the vertical red and blue dashed lines show the timings at which the Arase satellite footprint passed through the bright and dark MSTID parts, respectively.

The electric field variations of both DSI-x and DSI-y components in Figure 7c have peak-to-peak amplitudes of ∼0.4 mV/m, which is about half of those seen in Figure 6e in SM coordinates, indicating that the electric field measurements are dominantly on the spin plane and reliable. These electric field variations in Figure 7c and the airglow deviations show anti-correlations. In contrast, from Figure 7d, the DSI-x component and the DSI-y and DSI-z components of magnetic field variations are positively and negatively correlated with the airglow deviations, respectively. As a result, the field-aligned component (FA-z) of the Poynting

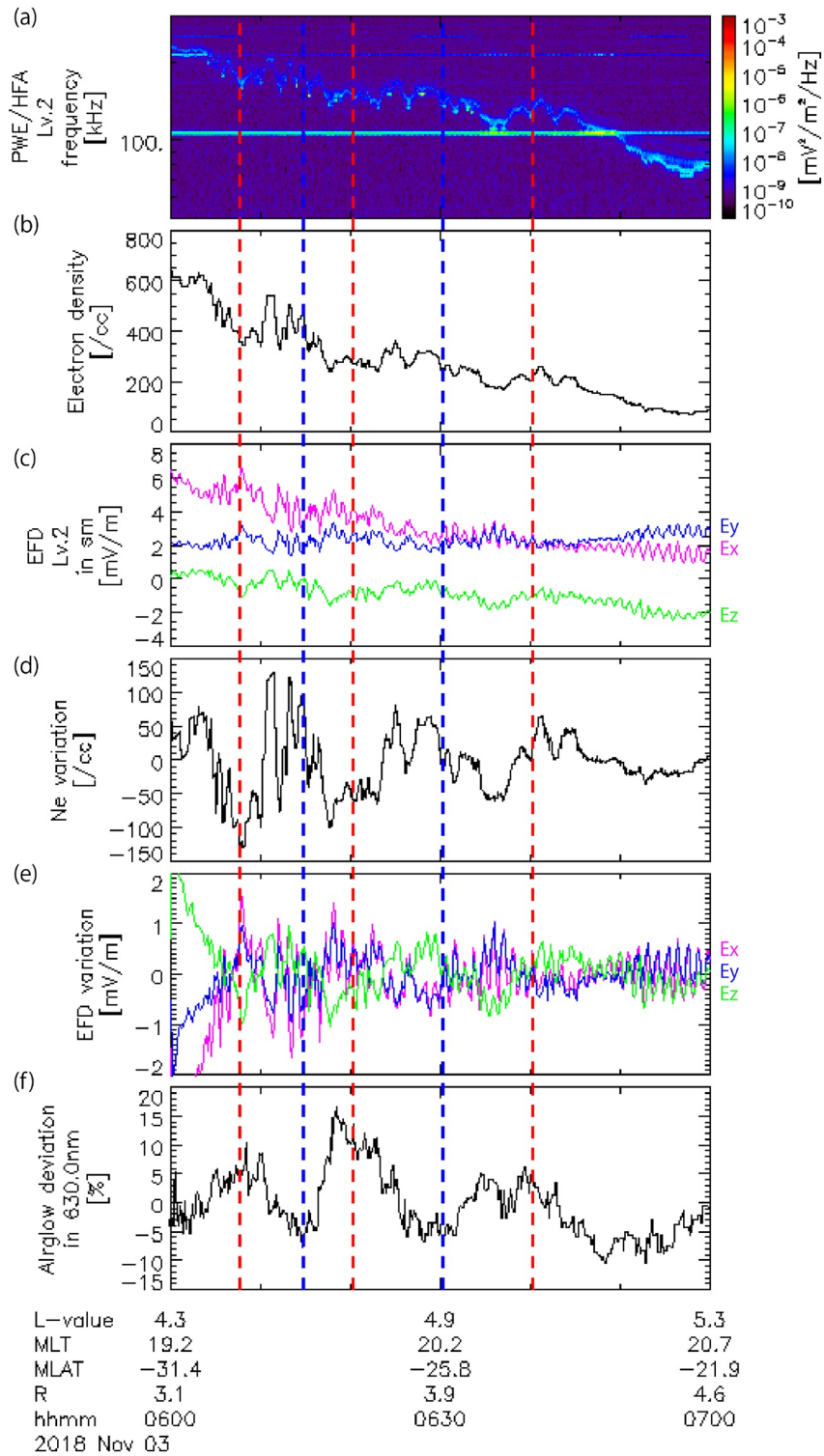

Figure 6. Airglow deviations at the Arase satellite footprint observed at Gakona, and the Arase satellite data observed at 0600–0700 UT on November 3, 2018 for (a) wave spectra, (b) electron density, (c) electric field measured by the u-sensor, (d) electron density variations, (f) electric field variations (δE), and (f) 630 nm airglow deviations at the Arase satellite. Variations in Figures 6d and 6e are calculated by subtracting 20 min running averages. Airglow deviations in Figure 6f were calculated by subtracting 1 h running averages. Vertical red and blue dashed lines show when the Arase satellite footprint passed through bright and dark parts of the medium-scale traveling ionospheric disturbance (MSTID), respectively.

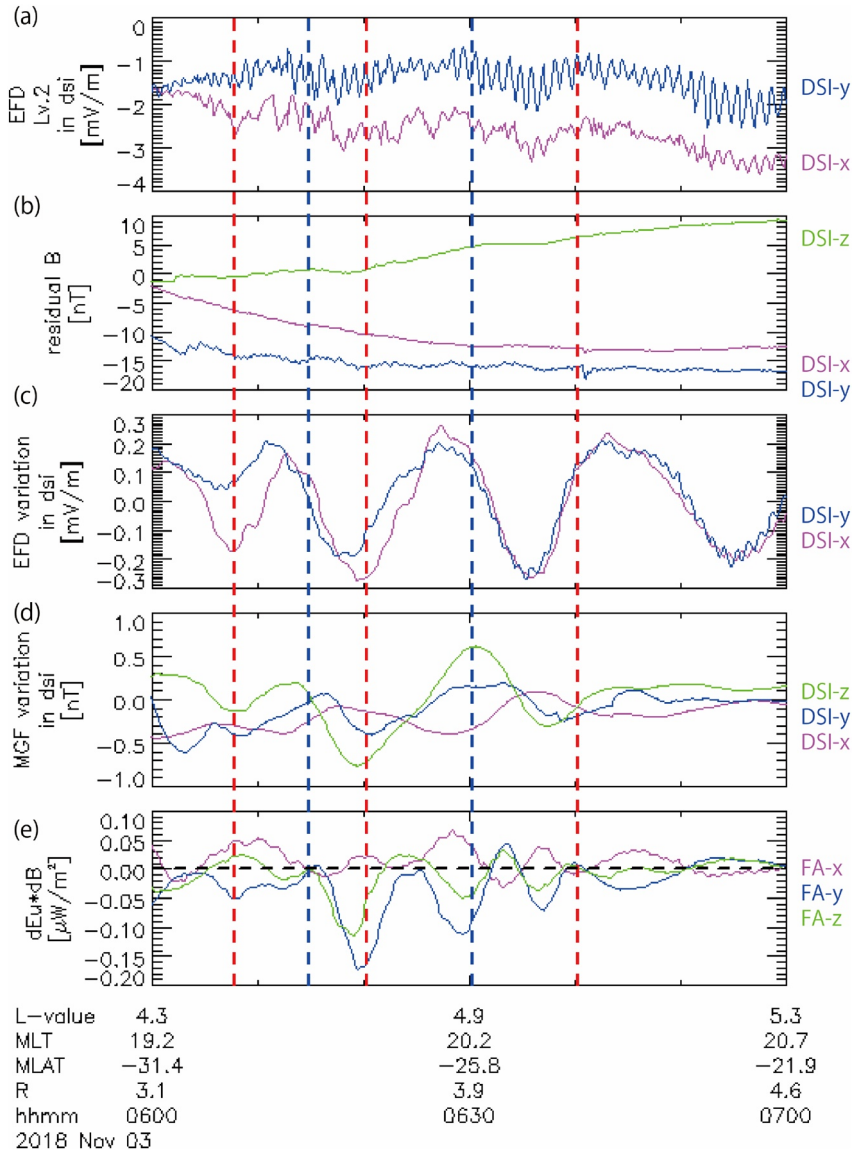

Figure 7. (a) Electric field measured by the u-sensor of EFD, (b) residual magnetic field obtained by subtracting the IGRF model magnetic field from the observed magnetic field, (c) electric field variations (δE), (d) magnetic field variations (δB), (e) Poynting vector calculated from δE and δB, observed by the Arase satellite from 0600–0700 UT on November 3, 2018. We calculated 5 min running averages, then 20 min running averages were further removed in Figures 7d and 7e. Vertical red and blue dashed lines show when the Arase satellite footprint passed through the bright and dark parts of the medium-scale traveling ionospheric disturbance, respectively.

vector in Figure 7e is mostly negative, meaning wave energy flows from the northern to the southern hemisphere. This Poynting vector was calculated assuming that the MSTID energy flows along the geomagnetic field lines as temporal variations of Alfven waves. The maximum value of the field-aligned Poynting vector was 0.11 $\mu W/m^2$ to the southern hemisphere. This may indicate that the observed MSTIDs were generated in the northern hemisphere through ionospheric instabilities, and the resultant polarization electric field was mapped to the southern hemisphere through the magnetic field line. However, note that the value of the field-aligned Poynting vector (FA-z) is comparable to those of the other two components (FA-x and FA-y), indicating that energy is not always propagating along the magnetic field line.

Next, we project electric field variations the Arase satellite observed in the inner magnetosphere onto the airglow images in the ionosphere. Assuming equipotential magnetic field lines, this is calculated as

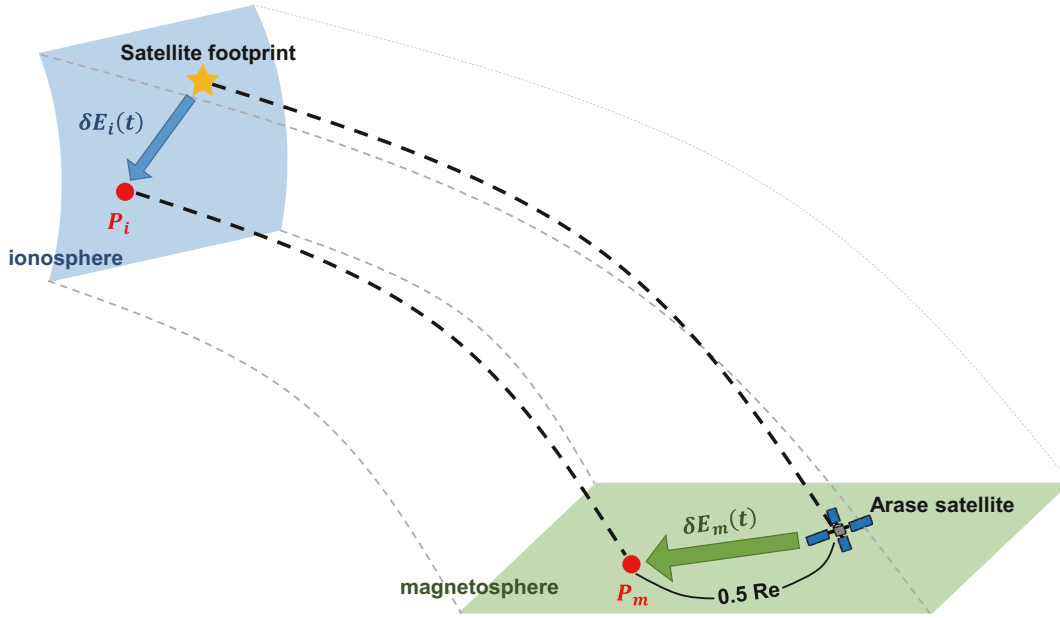

Figure 8. Schematic illustration of tracing procedure of electric field variation vectors from the magnetosphere to the ionosphere. The green and blue planes indicate the inner magnetosphere and the ionosphere. The black and gray dashed lines indicate the magnetic field lines. The yellow star indicates the footprint of the Arase satellite. The red dot on the inner magnetosphere plane (P_m) represent the position that is, 0.5 Re shifted from the Arase satellite position in the direction of the electric field variation vector. The green arrow shows the direction of the observed electric field variation vector. The red dot on the blue plane (P_i) represent the position where P_m is projected to at an altitude of 250 km in the ionosphere using the Tsyganenko–Sitnov 2005 magnetic field model. The blue arrow shows the direction of the mapped electric field variation vector.

$$\delta E_i(t) = \frac{r_m}{r_i}\delta E_m(t) \tag{1}$$

where $\delta E_m(t)$ and $\delta E_i(t)$ are the electric field variation in the inner magnetosphere and in the ionosphere, respectively, at time t, and r_m and r_i are the distance between the two magnetic field lines in the inner magnetosphere and in the ionosphere, respectively. Figure 8 is a schematic illustration showing the tracing procedure of electric field variation vectors from the inner magnetosphere to the ionosphere. The green and blue planes indicate the inner magnetosphere and the ionosphere, respectively, which are perpendicular to the ambient magnetic field. The black and gray dashed lines indicate the magnetic field lines. The yellow star indicates the footprint of the Arase satellite. The red dot P_m on the inner magnetosphere plane represent the position that is, 0.5 Re shifted from the Arase satellite position in the direction of the electric field variation vector. We mapped P_m to position P_i in the ionosphere by tracing the TS05 magnetic field. We defined the direction from the ionospheric footprint of Arase satellite to position P_i as the direction of the mapped electric field variation vector in the ionosphere, as shown by the blue arrow on the ionospheric plane.

In Figure 9, electric field variations at the ionospheric height as calculated by the above procedure are superimposed on images of the airglow deviations observed at Gakona. The black lines indicate electric field variation vectors projected onto the ionosphere from the electric field variations measured by the Arase. They are shown on the Arase satellite footprint trajectory. The yellow star is the Arase satellite footprint at each time frame. Please bear in mind that we can compare images of airglow deviations and electric field variations only around yellow star positions, because both the Arase and the MSTID are moving in time and space. Uncertainty of the Arase satellite footprint (~13 km if the altitude is shifted by 50 km) is approximately one order smaller than the horizontal wavelength of the MSTID (~165 km).

The resultant direction of the mapped electric field variation vectors points northwestward at the high airglow intensity region, while it points southeastward at the low airglow intensity region. In all three panels in Figure 9, the directions of electric field variations reverse when the Arase satellite footprint enters

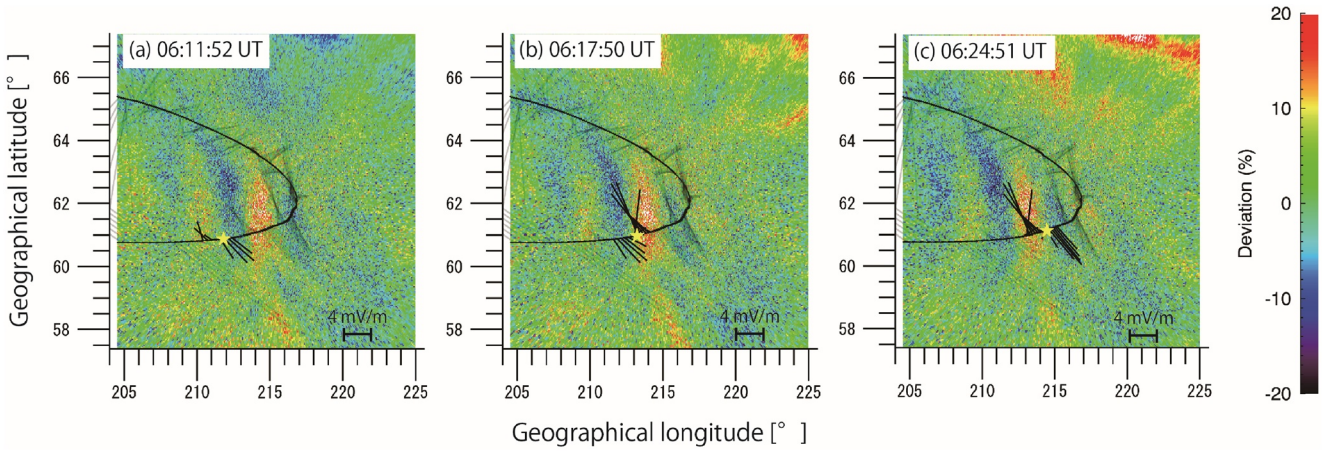

Figure 9. Comparison of airglow deviations and electric field variations in the ionosphere. Black lines are electric field variation vectors in the ionosphere, shown on the Arase satellite trajectory. The yellow star is the Arase satellite footprint at that time. The vertical and horizontal axis ranges are 57.76°–67.02° in latitudes and 204.78–224.78°E in longitudes, respectively, so that the actual north-south and east-west distances are nearly the same in these images, in order to avoid distortion of the wave front direction.

the region of opposite polarity in the airglow deviation. These features clearly indicate that the electric field variations observed by Arase is closely associated with MSTID structures. Previous literatures have suggested that the polarization electric field plays an important role in MSTID formation and growth (e.g., Shiokawa, Otsuka, et al., 2003). In this paper, we have provided first-ever observational evidence for the existence of the polarization electric field induced by MSTIDs on the basis of the direct measurement in the magnetosphere.

5. Discussion

The observed MSTID had a wavelength of ~165 km, a velocity of ~80 m/s, and a period of ~1 h. Shiokawa et al. (2013) statistically showed that MSTIDs at high latitudes (Tromsø, Norway and Athabasca, Canada) have characteristics of around 150–200 km wavelengths, 50–80 m/s velocities, and 30–60 min periods. At Athabasca, MSTIDs often show a north–south phase front propagating westward, indicating that the MSTID observed in this study has characteristics typical of those seen at high latitudes. The present event was observed during magnetically quiet condition (Kp = 0+) with the solar wind velocities of ~340–350 km and the northward interplanetary magnetic field of ~0.3–3.5 nT.

Figure 10 shows the configuration of the observed MSTID. Figures 10a and 10b are enlarged images of Figures 9a and 9b, zooming in on the geographic latitudes (59.0–63.0°N) and longitudes (208.0–216.0°E). Figures 10c and 10d show two schematic images of the MSTID structure.

The 630.0 nm airglow emission is caused by collisions of atomic oxygen ions (O^+) and oxygen molecules (O_2). If the ionosphere is lowered by some force, ion-neutral collisions occur more frequently, increasing the airglow intensity, and the Pedersen conductivity. If there is an eastward Pedersen current in the ionosphere, positive/negative charges are expected to accumulate on the east/west side of the bright airglow bands of the MSTID, because of the localized enhancement of the Pedersen conductivity. As a result, a westward polarization electric field is generated in the bright bands of the MSTID. This westward polarization electric field pushes the ionosphere downward by the $E \times B$ drift to increase the Pedersen conductivity, providing an ionospheric Perkins instability configuration.

From the above discussion, the polarization electric field is generated in the ionosphere as illustrated with the blue arrows in the bottom panels of Figure 10. The directions of these arrows are consistent with the zonal components of observed electric field variations shown in the upper panels of Figure 10. Consistency of the observed electric field variations and airglow variations holds not only in the two panels of Figures 10a and 10b, but also for other times during Arase crossing of the MSTID structure. We thus conclude that the polarization electric field associated with the MSTID in the ionosphere was projected to the

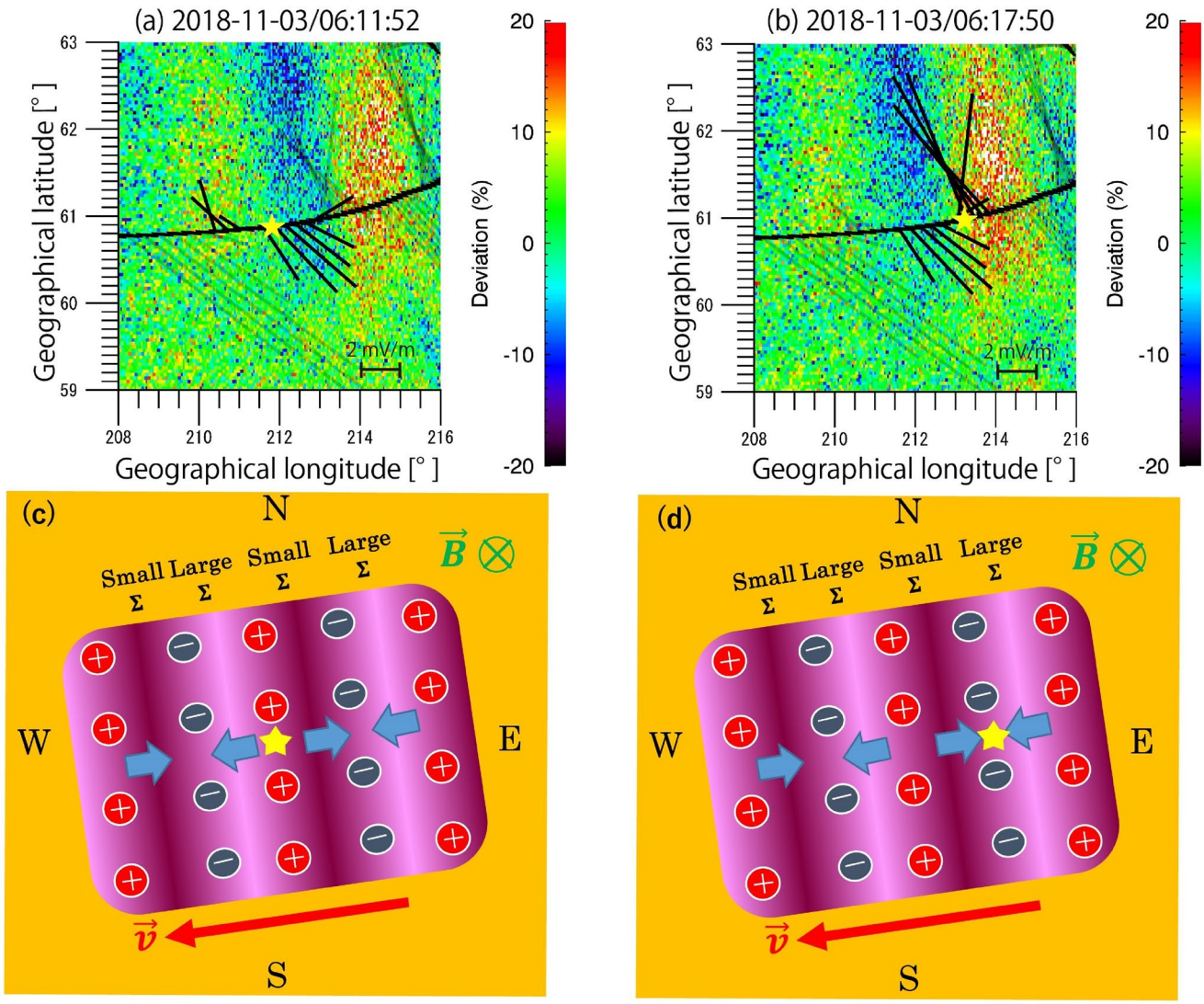

Figure 10. Panels (a) and (b) show the observed medium-scale traveling ionospheric disturbance (MSTID) phase front and directions of electric field variations in the ionosphere. Panels (c) and (d) are schematic images showing the generation mechanism of the polarization electric fields. Panels (c) and (d) are both shown in planes perpendicular to the magnetic field lines. In (c) and (d), the background orange square shows average Pedersen conductivity in the F-region ionosphere. Dark and light purple bands represent regions of low and high Pedersen conductivity, respectively (Σ: field-line integrated Pedersen conductivity). Red pluses and blue minuses indicate positive and negative charges, respectively. The green B vector ($\vec{B}$) and the red v vector ($\vec{v}$) indicate the direction of the magnetic field and the direction of MSTID propagation, respectively. The yellow star indicates the footprint position of the Arase satellite observing the electric field in the magnetosphere. Blue arrows indicate the direction of zonal components of the polarization electric field expected in this case.

magnetosphere and observed by the Arase satellite. This polarization electric field is probably caused by the spatial inhomogeneity of ionospheric Pedersen conductivity with the background eastward current in the ionosphere.

In Figure 10, we also observed rather significant meridional electric field. This may be caused by additional polarization electric field in the direction of MSTID phase front (north-south), as suggested by Kelley and Makela (2001), because the MSTID has a finite length in the meridional direction.

Figure 11a is a schematic illustration showing the electron density variation observed by the Arase satellite in the magnetosphere. The orange background indicates the ionosphere. The red pluses and blue minuses indicate positive and negative charges if the eastward Pedersen current flows in the F region ionosphere, respectively. The green B vector ($\vec{B}$), red v vector ($\vec{v}$), blue vector ($\delta\vec{E}$), and purple vector ($\delta\vec{E} \times \vec{B}$) indicate the magnetic field, MSTID propagation, zonal components of the polarization electric field, and the

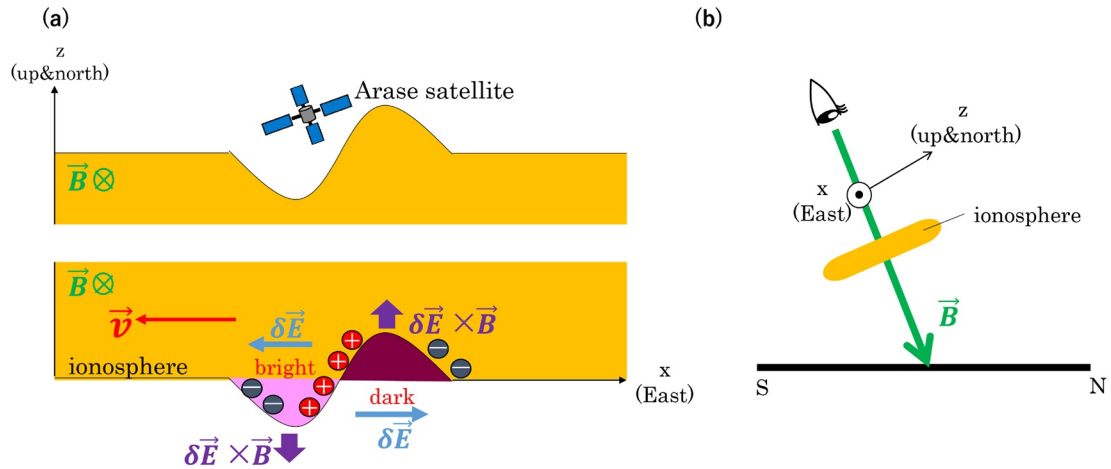

Figure 11. (a) A schematic illustration of the medium-scale traveling ionospheric disturbance (MSTID) growing process caused by the polarization electric field, as seen when one looks downward along the magnetic field to a plane perpendicular to the magnetic field, which is also illustrated in a horizontal view in Figure 11b. The x direction is eastward and z direction is upward and northward, both perpendicular to the magnetic field lines. Panel (a) illustrates both the bottom and top (near Arase) side of the ionosphere. The orange background indicates the ionosphere (conductive layer). Dark and light purple parts represent low and high Pedersen conductivities of MSTIDs due to upward and downward motion of the bottom side ionosphere, respectively, driven by $\delta\vec{E}\times\vec{B}$ drift. Red pluses and blue minuses indicate positive and negative charges, respectively. The green B vector ($\vec{B}$), red v vector ($\vec{v}$), blue vector ($\delta\vec{E}$), and purple vector ($\delta\vec{E}\times\vec{B}$) indicate the magnetic field, the propagation direction of the MSTID, zonal components of the polarization electric field, and the cross-product of $\delta\vec{E}$ and $\vec{B}$, respectively.

cross-component of $\delta\vec{E}$ and $\vec{B}$, respectively. This schematic shows the surface perpendicular to the magnetic field at the bottom side of the ionosphere and at the top side of the ionosphere at the Arase satellite. These bottom and top sides are connected by the same magnetic field lines. Figure 11b illustrates a side view of Figure 11a, looking westward from a position at east of the site.

At the bottom-side F-region ionosphere in Figure 11, an eastward and westward polarization electric fields are generated in the dark (low conductivity) and bright (high conductivity) airglow regions, respectively. This polarization electric field and magnetic field yield upward and downward component of $\delta\vec{E}\times\vec{B}$ drift, developing conductivity variations. When the F-region ionosphere moves upward/downward, electron density in the bottom-side F region decreases/increases, and airglow intensity decreases/increases, respectively. In the top-side ionosphere, including the magnetosphere, where the electron density decreases with increasing altitude, $\delta\vec{E}\times\vec{B}$ drift variations cause a negative correlation between the variations of airglow intensity and electron density, as shown in Figure 11a. As shown in Figures 5c and 6b, the Arase satellite observed the electron density decrease with increasing altitudes at $L = 4$–6, indicating that the density gradient is opposite to the bottom-side ionosphere. This scenario is consistent with observed negative correlation between airglow intensity and Arase electron density shown in Figures 6d and 6f, indicating that the polarization electric field associated with the MSTID caused the electron density variations in the magnetosphere.

Although the present observation missed the generation interval, the MSTID was probably generated by the polarization electric field in the ionosphere, because the observed electric field projected onto the ionosphere is consistent to the conductivity variations estimated from airglow variations with an eastward ionospheric current, as discussed above. One may argue that the growth rate of Perkins instability is small at high latitudes due to high magnetic inclination. However, the difference of the maximum growth rate at Gakona (inclination: 75.8°) from middle latitudes (inclination: 45°) would be only a factor of 2–3. If the growth develops to non-linear situation, the difference becomes further smaller. Thus, we consider that the ionospheric instabilities similar to those at middle latitudes, that is, E–F coupling and Perkins instabilities, can occur under the high inclination at Gakona.

At Gakona, an ionosonde has been operated by the Air Force Research Laboratory and available through Global Ionosphere Radio Observatory (Reinisch & Galkin, 2011). During the present MSTID event at 0600–0700 UT, the ionogram obtained at Gakona (not shown) did not show any appearance of the Es layer. This may contradict to the idea that the E-F coupling instability generates the observed MSTID. However, since

Es layer can occur at spatially small regions, there is a possibility that the ionosonde at Gakona missed the Es layer. Thus, we cannot completely deny the possibility of the E–F coupling instabilities for the present event.

It should be noted that we cannot also deny the possibility that the observed MSTID was caused not by ionospheric instabilities but by some magnetospheric processes. As shown in Figure 7e, the observed Poynting vector directed from the northern hemisphere to the southern hemisphere. The Arase satellite was in the southern hemisphere at −25 – −30 MLAT. This indicates that the electromagnetic energy came either from the ionosphere in the northern hemisphere or from the equatorial plane of the magnetosphere. In the latter case, the electric and magnetic field variations may be caused by some plasma instabilities in the magnetosphere, such as ballooning and/or interchange instabilities. Previous literatures suggested that these instabilities cause oscillating/wave-like auroral structures in the ionosphere (e.g., Motoba et al., 2012; Shiokawa et al., 2010, 2014). However, it is not likely that these instabilities occur during geomagnetically quiet conditions like in the present event. Because we did not observe the structures in the 557.7 nm images, as shown in Figures 3c and 3d, the present event is probably not the aurora caused by particle precipitation from the magnetosphere.

6. Conclusions

In this study, we reported the first simultaneous ground–magnetospheric satellite observation of an MSTID occurring on November 3, 2018, using a ground-based airglow imager (630.0 nm) at Gakona in Alaska and the Arase satellite. The results of this study are summarized as follows:

1. The MSTID had a north–south phase front and propagated westward with a horizontal wavelength of ∼165 km, a phase velocity of ∼80 m/s, and a period of ∼1 h. These values are typical of high-latitude MSTIDs.
2. The airglow intensity variations associated with the MSTID clearly correspond with the electric field variations and plasma density fluctuations observed by the Arase satellite. This indicates that the polarization electric field in the ionosphere associated with MSTID generation was projected to the magnetosphere and caused the electron density variation. Spatial inhomogeneity of the ionospheric Pedersen conductivity associated with the MSTID probably yields the polarization electric field.
3. We calculated the Poynting vector of the electric and magnetic field variations observed by the Arase satellite and associated with the MSTID. The field-aligned component of the Poynting vector was mostly negative, showing that wave energy flows from the northern to the southern hemisphere. The maximum value of the field-aligned Poynting vector was 0.11 $\mu W/m^2$. Note that the field-aligned component of the Poynting vector was comparable to those of the other two perpendicular components, suggesting that energy does not always propagate along the magnetic field line.

Data Availability Statement

Data from the PWING ground-based instruments are available at these websites. Science data of the ERG (Arase) satellite were obtained from the ERG Science Center operated by ISAS/JAXA and ISEE/Nagoya University (http://ergsc.isee.nagoya-u.ac.jp/, see Miyoshi, Hori, et al., 2018). The Arase satellite datasets for this research are available in these in-text data citation references: Asamura et al. (2018), Kasahara, Kasaba, et al. (2018), Kasahara, Kojima, et al. (2018), Kasahara, Kumamoto, et al. (2018), Kasahara, Yokota, et al. (2018), Matsuoka et al. (2018b), Miyoshi, Shinohara, and Jun (2018), Wang et al. (2018), and Yokota et al. (2018). The GIRO data resources are available at http://spase.info/SMWG/Observatory/GIRO.

Acknowledgments
The authors thank Yasuo Katoh, Yoshiyuki Hamaguchi, Yuka Yamamoto, and Takumi Adachi, technical staff of the ISEE at Nagoya University, for their helpful support when installing the ground-based instruments at Gakona, Alaska. The airglow camera installed at Gakona are optically calibrated at the National Institute of Polar Research (Ogawa et al., 2020). Database construction for the PWING ground-based instruments were supported by the ERG Science Center (https://ergsc.isee.nagoya-u.ac.jp/) and the Inter-university Upper atmosphere Global Observation Network (IUGONET) project (http://www.iugonet.org/). The development and operation of LEP-e was partly funded by Academia Sinica and National Cheng Kung University of Taiwan, and also through the support of the Ministry of Science and Technology of Taiwan under contracts 106-2111-M-001-011 and 105-3111-Y-001-042. The ionosonde at Gakona is operated by Air Force Research Laboratory, and provided by Terence W. Bullett through Global Ionosphere Radio Observatory (GIRO). This work was supported by JSPS KAKENHI [15H05815 (Y. Miyoshi), 16H06286 (K. Shiokawa and Y. Miyoshi), 20H01959 (Y. Miyoshi), 15H05747 (S. Oyama and Y. Miyoshi)].

References

Angelopoulos, V., Cruce, P., Drozdov, A., Grimes, E. W., Hatzigeorgiu, N., King, D. A., et al. (2019). The space physics environment data analysis system (SPEDAS). *Space Science Reviews*, *215*, 9. https://doi.org/10.1007/s11214-018-0576-4

Asamura, K., Miyoshi, Y., & Shinohara, I. (2018). *The LEPi instrument level-2 omni flux data of exploration of energization and radiation in geospace (ERG) Arase satellite* (Version v03_00). https://doi.org/10.34515/DATA.ERG-05001

Bärenzung, J., Holschneider, M., Wicht, J., Sanchez, S., Lesur, V., & Sanchez, S. (2020). The Kalmag model as a candidate for IGRF-13. *Earth Planets and Space*, *72*, 163. https://doi.org/10.1186/s40623-020-01295-y

Cosgrove, R. B., & Tsunoda, R. T. (2001). Polarization electric fields sustained by closed-current dynamo structures in midlatitude sporadic E. *Geophysical Research Letters*, *28*(8), 1455–1458. https://doi.org/10.1029/2000GL012178

Ejiri, M., Hoffman, R. A., & Smith, P. H. (1980). Energetic particle penetrations into the inner magnetosphere. *Journal of Geophysical Research*, *85*(A2), 653–663. https://doi.org/10.1029/JA085iA02p00653

Figueiredo, C. A. O. B., Takahashi, H., Wrasse, C. M., Otsuka, Y., Shiokawa, K., & Barros, D. (2018). Investigation of night time MSTIDs observed by optical thermosphere imagers at low latitudes: Morphology, propagation direction, and wind filtering. *Journal of Geophysical Research*, *123*, 7843–7857. https://doi.org/10.1029/2018JA025438

Fukao, S., Kelley, M. C., Shirakawa, T., Takami, T., Yamamoto, M., Tsuda, T., & Kato, S. (1991). Turbulent upwelling of the mid-latitude ionosphere, 1, Observational results by the MU radar. *Journal of Geophysical Research*, *96*(A3), 3725–3746. https://doi.org/10.1029/90JA02253

Garcia, F. J., Kelly, M. C., Makela, J. J., & Huang, C.–S. (2000). Airglow observations of mesoscale low-velocity traveling ionospheric disturbances in 630-nm airglow images over 7 years. *Journal of Geophysical Research*, *117*, A10324. https://doi.org/10.1029/2012JA017758

Hines, C. O. (1960). Internal atmospheric gravity waves at ionosphere heights. *Canadian Journal of Physics*, *38*(11), 1441–1481. https://doi.org/10.1139/p60-150

Hooke, W. H. (1968). Ionospheric irregularities produced by internal atmospheric gravity waves. *Journal of Atmospheric and Terrestrial Physics*, *30*(5), 795–823. https://doi.org/10.1016/S0021-9169(68)80033-9

Hunsuker, R. D. (1982). Atmospheric gravity waves generated in the high-latitude ionosphere: A review. *Reviews of Geophysics*, *20*(2), 293–315. https://doi.org/10.1029/RG020i002p00293

Kasahara, S., Yokota, S., Hori, T., Keika, K., Miyoshi, Y., & Shinohara, I. (2018). *The MEP-e instrument level-2 omni-directional flux data of exploration of energization and radiation in geospace (ERG) Arase satellite* (Version v01_02). ERG Science Center, Institute for Space-Earth Environmental Research, Nagoya University. https://doi.org/10.34515/DATA.ERG-02001

Kasahara, Y., Kasaba, Y., Matsuda, S., Shoji, M., Nakagawa, T., Ishisaka, K., et al. (2018). *The PWE/EFD instrument Level-2 spin-fit electric field data of exploration of energization and radiation in geospace (ERG) Arase satellite* (Version v04_01). ERG Science Center, Institute for Space-Earth Environmental Research, Nagoya University. https://doi.org/10.34515/DATA.ERG-07000

Kasahara, Y., Kojima, H., Matsuda, S., Ozaki, M., Yagitani, S., Shoji, M., et al. (2018). *The PWE/OFA instrument level-2 spectrum data of exploration of energization and radiation in geospace (ERG) Arase satellite* (Version v02_01). ERG Science Center, Institute for Space-Earth Environmental Research, Nagoya University. https://doi.org/10.34515/DATA.ERG-08000

Kasahara, Y., Kumamoto, A., Tsuchiya, F., Matsuda, S., Shoji, M., Nakamura, S., et al. (2018). *The PWE/HFA instrument Level-2 spectrum data of exploration of energization and radiation in geospace (ERG) Arase satellite* (Version v01_02). ERG Science Center, Institute for Space-Earth Environmental Research, Nagoya University. https://doi.org/10.34515/DATA.ERG-10000

Kelley, M. C., & Makela, J. J. (2001). Resolution of the discrepancy between experiment and theory of midlatitude F-region structures. *Geophysical Research Letters*, *28*, 2589–2592. https://doi.org/10.1029/2000GL012777

Martinis, C., Baumgardner, J., Wroten, J., & Mendillo, M. (2010). Seasonal dependence of MSTIDs obtained from 630.0 nm airglow imaging at Arecibo. *Geophysical Research Letters*, *37*, L11103. https://doi.org/10.1029/2010GL043569

Martinis, C., Baumgardner, J., Wroten, J., & Mendillo, M. (2017). All-sky-imaging capabilities for ionospheric space weather research using geomagnetic conjugate point observing sites. *Advances in Space Research*, *61*, 1636–1651. https://doi.org/10.1016/j.asr.2017.07.021

Matsuoka, A., Teramoto, M., Imajo, S., Kurita, S., Miyoshi, Y., & Shinohara, I. (2018a). *The MGF instrument Level-2 spinfit magnetic field data of Exploration of energization and Radiation in Geospace (ERG) Arase satellite* (Version v03.04). ERG Science Center, Institute for Space-Earth Environmental Research, Nagoya University. https://doi.org/10.34515/DATA.ERG-06001

Matsuoka, A., Teramoto, M., Imajo, S., Kurita, S., Miyoshi, Y., & Shinohara, I. (2018b). *The MGF instrument Level-2 high-resolution magnetic field data of Exploration of energization and Radiation in Geospace (ERG) Arase satellite* (Version v03_04). ERG Science Center, Institute for Space-Earth Environmental Research, Nagoya University. https://doi.org/10.34515/DATA.ERG-06000

Miyoshi, Y., Hori, T., Shoji, M., Teramoto, M., Chang, T. F., Segawa, T., et al. (2018). The ERG science center. *Earth Planets and Space*, *70*, 96. https://doi.org/10.1186/s40623-018-0867-8

Miyoshi, Y., Shinohara, I., & Jun, C.-W. (2018). Updated daily. *The Level-2 orbit data of Exploration of energization and Radiation in Geospace (ERG) Arase satellite, Version v03*. ERG science center, Institute for Space-Earth Environmental Research, Nagoya University. https://doi.org/10.34515/DATA.ERG-12000

Miyoshi, Y., Shinohara, I., Takashima, T., Asamura, K., Higashio, N., Mitani, T., et al. (2018). Geospace exploration project ERG. *Earth Planets and Space*, *70*, 101. https://doi.org/10.1186/s40623-018-0862-0

Motoba, T., Hosokawa, K., Kadokura, A., & Sato, N. (2012). Magnetic conjugacy of northern and southern auroral beads. *Geophysical Research Letters*, *39*, L08108. https://doi.org/10.1029/2012GL051599

Ogawa, Y., Kadokura, A., & Ejiri, M. K. (2020). Optical calibration system of NIPR for aurora and airglow observations. *Polar Science*, *26*, 100570. https://doi.org/10.1016/j.polar.2020.100570

Otsuka, Y., Shiokawa, K., Ogawa, T., & Wilkinson, P. (2004). Geomagnetic conjugate observations of medium-scale traveling ionospheric disturbances at midlatitude using all sky imagers. *Geophysical Research Letters*, *31*, L15803. https://doi.org/10.1029/2004GL020262

Otsuka, Y., Suzuki, K., Nakagawa, S., Nishioka, M., Shiokawa, K., & Tsugawa, T. (2013). GPS observations of medium-scale traveling ionospheric disturbances over Europe. *Annales Geophysicae*, *31*(2), 163–172. https://doi.org/10.5194/angeo-31-163-2013

Perkins, F. (1973). Spread F and ionospheric currents. *Journal of Geophysical Research*, *78*, 218–226. https://doi.org/10.1029/JA078i001p00218

Reinisch, B. W., & Galkin, I. A. (2011). Global ionospheric radio observatory (GIRO). *Earth Planets and Space*, *63*, 377–381. https://doi.org/10.5047/eps.2011.03.001

Shiokawa, K., Hashimoto, A., Hori, T., Sakaguchi, K., Ogawa, Y., Donovan, E., et al. (2014). Auroral fragmentation into patches. *Journal of Geophysical Research: Space Physics*, *119*, 8249–8261. https://doi.org/10.1002/2014JA020050

Shiokawa, K., Ihara, C., Otsuka, Y., & Ogawa, T. (2003). Statistical study of night time medium-scale traveling ionospheric disturbances using midlatitude airglow images. *Journal of Geophysical Research*, *108*(A1), 1052. https://doi.org/10.1029/2002JA009491

Shiokawa, K., Katoh, Y., Hamaguchi, Y., Yamamoto, Y., Adachi, T., Ozaki, M., et al. (2017). Ground-based instruments of the PWING project to investigate dynamics of the inner magnetosphere at subauroral latitudes as a part of the ERG-ground coordinated observation network. *Earth Planets and Space*, *69*, 160. https://doi.org/10.1186/s40623-017-0745-9

Shiokawa, K., Katoh, Y., Satoh, M., Ejiri, M. K., Ogawa, T., Nakamura, T., et al. (1999). Development of optical mesosphere thermosphere imagers (OMTI). *Earth Planets and Space*, *51*, 887–896. https://doi.org/10.1186/BF03353247

Shiokawa, K., Mori, M., Otsuka, Y., Oyama, S., Nozawa, S., Suzuki, S., & Connors, M. (2013). Observation of night time medium-scale traveling ionospheric disturbances by two 630-nm airglow imagers near the auroral zone. *Journal of Atmospheric and Solar-Terrestrial Physics*, *103*, 184–194. https://doi.org/10.1016/j.jastp.2013.03.024

Shiokawa, K., Nakajima, A., Ieda, A., Sakaguchi, K., Nomura, R., Aslaksen, T., et al. (2010). Rayleigh-Taylor type instability in auroral patches. *Journal of Geophysical Research*, *115*, A02211. https://doi.org/10.1029/2009ja014273

Shiokawa, K., Otsuka, Y., Ihara, C., Ogawa, T., & Rich, F. J. (2003). Ground and satellite observations of night time medium-scale traveling ionospheric disturbance at midlatitude. *Journal of Geophysical Research*, *108*(A4), 1145. https://doi.org/10.1029/2002JA009639

Shiokawa, K., Otsuka, Y., Tsugawa, T., Ogawa, T., Saito, A., Ohshima, K., et al. (2005). Geomagnetic conjugate observation of night time medium-scale and large-scale traveling ionospheric disturbances: FRONT3 campaign. *Journal of Geophysical Research*, *110*, A05303. https://doi.org/10.1029/2004JA010845

Smith, P. H., & Hoffman, R. A. (1974). Direct observations in the dusk hours of the characteristics of the storm time ring current particles during the beginning of magnetic storms. *Journal of Geophysical Research*, *79*(7), 966–971. https://doi.org/10.1029/JA079i007p00966

Tsyganenko, N. A., & Sitnov, M. I. (2005). Modeling the dynamics of the inner magnetosphere during strong geomagnetic storms. *Journal of Geophysical Research*, *110*, A03208. https://doi.org/10.1029/2004JA010798

Wang, S.-Y., Kazama, Y., Jun, C.-W., Chang, T.-F., Hori, T., Miyoshi, Y., & Shinohara, I. (2018). *The LEPe instrument level-2 omni-directional flux data of exploration of energization and radiation in geospace (ERG) Arase satellite* (Version v02_02). ERG Science Center, Institute for Space-Earth Environmental Research, Nagoya University. https://doi.org/10.34515/DATA.ERG-04002

Yokota, S., Kasahara, S., Hori, T., Keika, K., Miyoshi, Y., & Shinohara, I. (2018). *The MEP-i instrument Level-2 omni-directional flux data of exploration of energization and radiation in geospace (ERG) Arase satellite* (Version v02_00). ERG Science Center, Institute for Space-Earth Environmental Research, Nagoya University. https://doi.org/10.34515/DATA.ERG-03001

Yokoyama, T., Hysell, D. L., Otsuka, Y., & Yamamoto, M. (2009). Three-dimensional simulation of the coupled Perkins and Es-layer instabilities in the night time midlatitude ionosphere. *Journal of Geophysical Research*, *114*, A03308. https://doi.org/10.1029/2008JA013789